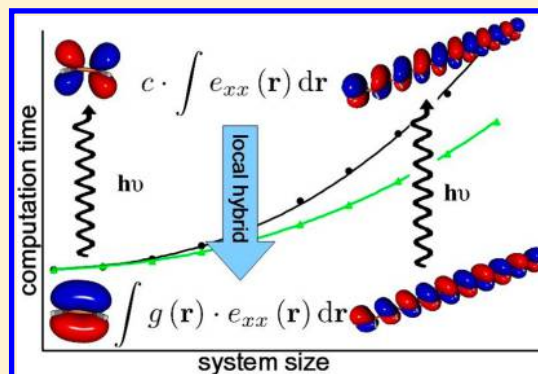


Efficient Semi-numerical Implementation of Global and Local Hybrid Functionals for Time-Dependent Density Functional Theory

Toni M. Maier, Hilke Bahmann,* and Martin Kaupp*

Institut für Chemie Theoretische Chemie/Quantenchemie, Technische Universität Berlin, Sekr. C7 Straße des 17. Juni 135, D-10623, Berlin, Germany

ABSTRACT: Local hybrid functionals with position-dependent exact-exchange admixture offer increased flexibility compared to global hybrids. For sufficiently advanced functionals of this type, this is expected to hold also for a wide range of electronic excitations within time-dependent density functional theory (TDDFT). Following a recent semi-numerical implementation of local hybrid functionals for ground-state self-consistent-field calculations (Bahmann, H.; Kaupp, M. *J. Chem. Theory Comput.* 2015, 11, 1540–1548), the first linear-response TDDFT implementation of local hybrids is reported, using a semi-numerical integration technique. The timings and accuracy of the semi-numerical implementation are evaluated by comparison with analytical schemes for time-dependent Hartree–Fock (TDHF) and for the TPSSH global hybrid. In combination with the RI approximation to the Coulomb part of the kernel, the semi-numerical implementation is faster than the existing analytical TDDFT/TDHF implementation of global hybrid functionals in the TURBOMOLE code, even for small systems and moderate basis sets. Moreover, timings for global and local hybrids are practically equal for the semi-numerical scheme. The way to TDDFT calculations with local hybrid functionals for large systems is thus now open, and more sophisticated parametrizations of local hybrids may be evaluated.



1. INTRODUCTION

Over the last 2 decades, linear-response time-dependent density-functional theory (TDDFT) with adiabatic exchange–correlation kernels has become the work horse for calculations of electronic excitation spectra in quantum chemistry¹ as well as in solid-state research.^{2–5} The main reason for this is the excellent ratio between accuracy and computational effort.⁶ In contrast to purely wave function-based methods such as CASSCF, CASPT2, MRCI, EOM-CCSD, CC2, and others, significantly larger molecules (or unit cells) are accessible.⁷

Known shortcomings of TDDFT with semi-local functionals, such as for charge-transfer, Rydberg, or core excitations,^{8–10} have been overcome to a certain extent by using hybrid schemes that incorporate exact exchange from the Hartree–Fock approximation. Global hybrid functionals¹¹ with a constant fraction of the exact-exchange (EXX) energy combined with semi-local (sl) or purely local exchange and correlation energies represent the basic formulation of such a hybrid scheme

$$E_{xc}^{GH} = E_c^{sl} + \sum_{\sigma=\alpha,\beta} [cE_{x,\sigma}^{ex} + (1-c)E_{x,\sigma}^{sl}] \quad (1)$$

where the exact-exchange energy is given in terms of the occupied molecular spin orbitals $\{\varphi_{k_\sigma}\}$

$$E_{x,\sigma}^{ex} = -\frac{1}{2} \sum_{kl}^{occ} \iint \frac{\varphi_{k_\sigma}^*(\mathbf{r}) \varphi_{l_\sigma}(\mathbf{r}) \varphi_{l_\sigma}^*(\mathbf{r}') \varphi_{k_\sigma}(\mathbf{r}')}{|\mathbf{r} - \mathbf{r}'|} d\mathbf{r} d\mathbf{r}' \quad (2)$$

The optimal value for c , the EXX admixture, however, has been recognized to vary strongly for different types of excitations, as it is known to do even for different ground-state properties (e.g., for thermochemistry vs reaction barriers).^{12,13} For example, valence excitations are usually well-described by (semi)local functionals or the B3LYP functional with 20% EXX, whereas more EXX is needed for core- and charge-transfer excitations.^{14–16} This has, e.g., led to schemes using different values of c for core–core, core–valence, and valence–valence interactions.¹⁷ A more flexible way of admixing EXX in density functionals is achieved in range-separated functionals.^{18–27} In particular, long-range corrected functionals that exhibit full EXX at large interelectronic distances account for the correct asymptotic behavior and thus improve charge-transfer and Rydberg excitations.^{15,25} The constant range-separation parameter, however, has been identified as a limitation to the general applicability of range hybrids. For example, nonempirical tuning of range hybrids to minimize delocalization errors showed that the optimal range-separation length increases with increasing chromophore size.²⁸

Received: June 30, 2015

Published: August 14, 2015

Moreover, if one wants to avoid size-consistency problems,²⁹ an averaging over individually tuned range-separation lengths is unavoidable.³⁰ To describe core excitations accurately, EXX is additionally required at shorter ranges.

Another extension to global hybrids, which so far has not entered the TDDFT arena, is local hybrid functionals^{31,32}

$$E_{xc}^{LH} = \sum_{\sigma=\alpha,\beta} \int g_{\sigma}(\mathbf{r}) \cdot e_{x,\sigma}^{ex}(\mathbf{r}) d\mathbf{r} + \sum_{\sigma=\alpha,\beta} \int [1 - g_{\sigma}(\mathbf{r})] \cdot e_{x,\sigma}^{sl}(\mathbf{r}) d\mathbf{r} + E_c^{sl} \quad (3)$$

where the constant mixing parameter is substituted by a real-space quantity, the so-called local mixing function (LMF) $g_{\sigma}(\mathbf{r})$. e_x represents a (semi)local exchange-energy density. The EXX energy density in the conventional gauge is defined as

$$e_{x,\sigma}^{ex}(\mathbf{r}) = -\frac{1}{2} \sum_{kl}^{\text{occ}} \int \frac{\varphi_{k\sigma}^*(\mathbf{r}) \varphi_{l\sigma}(\mathbf{r}) \varphi_{l\sigma}^*(\mathbf{r}') \varphi_{k\sigma}(\mathbf{r}')}{|\mathbf{r} - \mathbf{r}'|} d\mathbf{r}' \quad (4)$$

Local hybrids have been assessed successfully for ground-state properties, showing their tremendous potential for atomization energies, reaction barriers, and other properties.^{33–35} By construction, an appropriate LMF can provide full exact-exchange asymptotically, whereas lower values of the LMF in bonding regions can bring in static correlation effects at the same time. The former property plays an important role for the description of Rydberg excitations, while the latter is needed for calculations of valence excitations. Moreover, an ideal LMF is expected to exhibit large EXX admixtures near the nuclei. This should enable accurate results also for core excitations. Local hybrid functionals are thus expected to be able to provide good performance for very different types of excitations in molecules or solids. As there has so far been no TDDFT implementation of local hybrid functionals, no numerical proof of this expectation has been possible. Recently, we have shown that the local hybrid potential can be implemented efficiently using a semi-numerical scheme.³⁶ The final cost of a self-consistent local hybrid calculation is comparable to that of a global hybrid calculation. Extending this work, we report here the first linear-response TDDFT implementation of local hybrids, along with an efficient semi-numerical TDDFT implementation of global hybrids in the TURBOMOLE program. Previous semi-numerical TDDFT implementations of global hybrids using pseudospectral methods or the RIJ-COSX approach are available but had been limited to the Tamm–Dancoff approximation (TDA).^{37,38}

First, the local hybrid exchange-correlation kernel within the framework of linear-response TDDFT will be derived. After outlining the semi-numerical integration scheme for integrals related to EXX in local and global hybrids, we describe the details of our implementation. The numerical accuracy and efficiency of the approach will be discussed in detail, both for local and global hybrid functionals. In the latter case, timings will be directly compared to the existing analytical implementation of global hybrids for TDDFT within the TURBOMOLE package, and the local hybrid implementation will be compared to both global hybrid implementations. We emphasize that a systematic evaluation of the performance of different local hybrids in TDDFT is outside the scope of the present work and will be reported elsewhere.

2. THEORY

2.1. Linear-Response TDDFT. In the framework of linear-response TDDFT (see reviews in refs 1 and 39 for more details), excitation energies ω are characterized as the poles of the response function. Hence, they can be calculated as the eigenvalues of the non-Hermitian supermatrix equation

$$\begin{pmatrix} L & M \\ M^* & L^* \end{pmatrix} \begin{pmatrix} X \\ Y \end{pmatrix} = \omega \begin{pmatrix} 1 & 0 \\ 0 & -1 \end{pmatrix} \begin{pmatrix} X \\ Y \end{pmatrix} \quad (5)$$

with X and Y being transition-density matrices describing the excitation and de-excitation processes, respectively. For a real wave function, which can be assumed in the absence of a magnetic field or of spin–orbit coupling, L and M are real-valued matrices. Equation 5 thus decomposes into a set of linear equations

$$(L \pm M)(X \pm Y) = \omega(X \mp Y) \quad (6)$$

that are solved iteratively.⁴⁰ Matrices $L + M$ and $L - M$ are denoted electric and magnetic orbital-rotation Hessian, respectively. Their products with the transition density matrices $(X \pm Y)$ are called matrix–vector products V^{\pm} . For spin-resolved kernels (σ and ς as spin indices), they are defined as

$$V_{ia\sigma}^{\pm} = \sum_{jb\varsigma} (L \pm M)_{ia\sigma,jb\varsigma} (X \pm Y)_{jb\varsigma} \quad (7)$$

In the usual nomenclature, i, j, \dots for occupied orbitals, a, b, \dots for virtual orbitals, p, q, \dots for general orbitals, and σ, σ' as spin indices, the orbital-rotation Hessians are defined as

$$(L + M)_{ia\sigma,jb\sigma'} = \delta_{ij}\delta_{ab}\delta_{\sigma\sigma'}(\epsilon_{a\sigma} - \epsilon_{i\sigma}) + 2(i_{\sigma}a_{\sigma}|b_{\sigma'}j_{\sigma'}) + (i_{\sigma}a_{\sigma}|f_{xc}^{\sigma\sigma'}|b_{\sigma'}j_{\sigma'}) + (i_{\sigma}a_{\sigma}|f_{xc}^{\sigma\sigma'}|j_{\sigma'}b_{\sigma'}) \quad (8)$$

$$(L - M)_{ia\sigma,jb\sigma'} = \delta_{ij}\delta_{ab}\delta_{\sigma\sigma'}(\epsilon_{a\sigma} - \epsilon_{i\sigma}) + (i_{\sigma}a_{\sigma}|f_{xc}^{\sigma\sigma'}|b_{\sigma'}j_{\sigma'}) - (i_{\sigma}a_{\sigma}|f_{xc}^{\sigma\sigma'}|j_{\sigma'}b_{\sigma'}) \quad (9)$$

Following the definitions by Casida,³⁹ the exchange-correlation kernel integrals $(i_{\sigma}a_{\sigma}|f_{xc}^{\sigma\sigma'}|b_{\sigma'}j_{\sigma'})$ and $(i_{\sigma}a_{\sigma}|f_{xc}^{\sigma\sigma'}|j_{\sigma'}b_{\sigma'})$ are defined as derivatives of exchange-correlation Fock matrix elements with respect to the density matrix \mathbf{D}

$$(i_{\sigma}a_{\sigma}|f_{xc}^{\sigma\sigma'}|b_{\sigma'}j_{\sigma'}) = \frac{\partial F_{ia\sigma}^{xc}}{\partial D_{jb\sigma'}} \quad (10)$$

$$(i_{\sigma}a_{\sigma}|f_{xc}^{\sigma\sigma'}|j_{\sigma'}b_{\sigma'}) = \frac{\partial F_{ia\sigma}^{xc}}{\partial D_{bj\sigma'}} \quad (11)$$

For semi-local functionals and in the adiabatic limit, the exchange-correlation kernel $f_{xc}^{\sigma\sigma'}$ is equivalently expressed as the second functional derivative of the time-independent exchange-correlation energy with respect to the electron density

$$(i_{\sigma}a_{\sigma}|f_{xc}^{\sigma\sigma'}|b_{\sigma'}j_{\sigma'}) = \iint \varphi_{i\sigma}^*(\mathbf{r}_1) \varphi_{a\sigma}(\mathbf{r}_1) \frac{\delta^2 E_{xc}}{\delta \rho_{\sigma}(\mathbf{r}_1) \delta \rho_{\sigma'}(\mathbf{r}_2)} \varphi_{b\sigma'}(\mathbf{r}_2) \varphi_{j\sigma'}^*(\mathbf{r}_2) d\mathbf{r}_1 d\mathbf{r}_2 \quad (12)$$

$$(i_{\sigma} a_{\sigma} f_{xc}^{\sigma\sigma'} | j_{\sigma'} b_{\sigma'}) = \int \int \varphi_{i_{\sigma}}^*(\mathbf{r}_1) \varphi_{a_{\sigma}}(\mathbf{r}_1) \frac{\delta^2 E_{xc}}{\delta \rho_{\sigma}(\mathbf{r}_1) \delta \rho_{\sigma'}(\mathbf{r}_2)} \varphi_{j_{\sigma'}}(\mathbf{r}_2) \varphi_{b_{\sigma'}}^*(\mathbf{r}_2) d\mathbf{r}_1 d\mathbf{r}_2 \quad (13)$$

For occupied-orbital-dependent functionals like kinetic-energy dependent meta-GGAs, current-density-dependent functionals,⁴¹ or hybrid functionals, the Fock matrix elements are calculated in a generalized Kohn–Sham (GKS) framework (used throughout this work), where the exchange-correlation potential is replaced by a functional derivative with respect to the orbitals.⁴² Considering the relation between the density and the density matrix given by⁴³

$$\rho_{\sigma}(\mathbf{r}) = \sum_{pq} D_{pq\sigma} \varphi_p^*(\mathbf{r}) \varphi_q(\mathbf{r}) \quad (14)$$

equations 12 and 13 are readily obtained from eqs 10 and 11. Explicit formulas for (semi)local kernel integrals can be found in the literature for GGAs and meta-GGAs.^{40,44} In ref 44, the meta-GGA kernel is derived as a second functional derivative of the exchange-correlation energy with respect to the orbitals. These expressions can also be obtained by taking into account the dependence of the kinetic energy density on the density matrix

$$\tau_{\sigma}(\mathbf{r}) = \frac{1}{2} \sum_{pq\sigma} D_{pq\sigma} \nabla \varphi_p^*(\mathbf{r}) \cdot \nabla \varphi_q(\mathbf{r}) \quad (15)$$

2.2. Local Hybrid Exchange Kernel. For simplicity, we will focus on the exchange contribution and suppress spin indices, considering a spin-resolved LMF that depends on the density ρ , the square of the density gradient γ , and the kinetic-energy density τ . The total exchange energy is the sum of α and β exchange, and cross terms arise only in the correlation part. The following quantities thus represent only one spin contribution, keeping in mind that for open-shell systems α and β contributions have to be calculated separately. The correlation contribution to the exchange-correlation kernel integrals can be derived following the usual procedure for (semi)local functionals (cf. eqs 12 and 13). It can be subsequently added to the LH exchange part. Following the derivation of the LH exchange potential that is described in detail in ref 42, the corresponding exchange contributions to the Fock matrix are given by

$$F_{ia}^x = \int [e_x^{\text{ex}}(\mathbf{r}) - e_x^{\text{sl}}(\mathbf{r})] \hat{d}_{ia} g(\mathbf{r}) d\mathbf{r} + \int [1 - g(\mathbf{r})] \hat{d}_{ia} e_x^{\text{sl}} d\mathbf{r} + \frac{1}{2} \int \varphi_i^*(\mathbf{r}) [g(\mathbf{r}) \hat{v}_x^{\text{ex}} \varphi_a(\mathbf{r}) + \hat{v}_x^{\text{ex}}(g \varphi_a)(\mathbf{r})] d\mathbf{r} \quad (16)$$

where semi-local potential terms are abbreviated by introducing the differential operators \hat{d}_{pq} . They can be thought of as semi-local potential operators resulting from the differentiation of either the LMF or the semi-local exchange-energy density with respect to density-matrix elements D_{pq} . Choosing exemplarily the action on the LMF, \hat{d}_{pq} is defined by

$$\hat{d}_{pq} g(\mathbf{r}) = \varphi_p^*(\mathbf{r}) \varphi_q(\mathbf{r}) \frac{\partial g}{\partial \rho}(\mathbf{r}) + 2 \nabla \rho(\mathbf{r}) \cdot \nabla (\varphi_p^*(\mathbf{r}) \varphi_q(\mathbf{r})) \frac{\partial g}{\partial \gamma}(\mathbf{r}) + \frac{1}{2} \nabla \varphi_p^*(\mathbf{r}) \cdot \nabla \varphi_q(\mathbf{r}) \frac{\partial g}{\partial \tau}(\mathbf{r}) \quad (17)$$

Note that in the last term of eq 16 the nonlocal exact-exchange potential acts on both the LMF and the orbital. The exact-

exchange energy density and the nonlocal exact-exchange potential are related to the density matrix in the following way

$$e_x^{\text{ex}}(\mathbf{r}) = -\frac{1}{2} \sum_{pqrs} D_{pq} D_{rs} \int \frac{\varphi_q^*(\mathbf{r}) \varphi_r(\mathbf{r}) \varphi_s^*(\mathbf{r}') \varphi_p(\mathbf{r}')}{|\mathbf{r} - \mathbf{r}'|} d\mathbf{r}' \quad (18)$$

$$\hat{v}_x^{\text{ex}} \varphi_p(\mathbf{r}) = -\sum_{rs} D_{rs} \int \int \frac{\varphi_r(\mathbf{r}) \varphi_s^*(\mathbf{r}') \varphi_p(\mathbf{r}')}{|\mathbf{r} - \mathbf{r}'|} d\mathbf{r}' \quad (19)$$

Defining the exchange-kernel integrals as the derivative of the exchange contribution to the Fock matrix with respect to the density matrix

$$(ialf_x | bj) = \frac{\partial F_{ia}^x}{\partial D_{jb}} \quad (20)$$

$$(ialf_x | jb) = \frac{\partial F_{ia}^x}{\partial D_{bj}} \quad (21)$$

and inserting the local hybrid exchange Fock-matrix element from eq 16 gives the local hybrid exchange-kernel integrals

$$(ialf_x^{\text{LH}} | jb) = -\frac{1}{2} \int \int [g(\mathbf{r}_1) + g(\mathbf{r}_2)] \frac{\varphi_i^*(\mathbf{r}_1) \varphi_a(\mathbf{r}_2) \varphi_j(\mathbf{r}_1) \varphi_b^*(\mathbf{r}_2)}{|\mathbf{r}_1 - \mathbf{r}_2|} d\mathbf{r}_1 d\mathbf{r}_2 - \frac{1}{2} \int \int \hat{d}_{ij} [g(\mathbf{r}_1) + g(\mathbf{r}_2)] \sum_k \frac{\varphi_i^*(\mathbf{r}_2) \varphi_a(\mathbf{r}_1) \varphi_k^*(\mathbf{r}_1) \varphi_k(\mathbf{r}_2)}{|\mathbf{r}_1 - \mathbf{r}_2|} d\mathbf{r}_1 d\mathbf{r}_2 - \frac{1}{2} \int \int \hat{d}_{ia} [g(\mathbf{r}_1) + g(\mathbf{r}_2)] \sum_k \frac{\varphi_j(\mathbf{r}_1) \varphi_b^*(\mathbf{r}_2) \varphi_k(\mathbf{r}_1) \varphi_k^*(\mathbf{r}_2)}{|\mathbf{r}_1 - \mathbf{r}_2|} d\mathbf{r}_1 d\mathbf{r}_2 - \frac{1}{2} \int \int \hat{d}_{ia} \hat{d}_{jb} g(\mathbf{r}_1) \sum_{kl} \frac{\varphi_k^*(\mathbf{r}_1) \varphi_k(\mathbf{r}_2) \varphi_l(\mathbf{r}_1) \varphi_l^*(\mathbf{r}_2)}{|\mathbf{r}_1 - \mathbf{r}_2|} d\mathbf{r}_1 d\mathbf{r}_2 + \int [\{1 - g(\mathbf{r}_1)\} \hat{d}_{ia} \hat{d}_{jb} e_x^{\text{sl}}(\mathbf{r}_1) - \hat{d}_{ia} \hat{d}_{jb} g(\mathbf{r}_1) e_x^{\text{sl}}(\mathbf{r}_1)] d\mathbf{r}_1 - \int [\hat{d}_{jb} g(\mathbf{r}_1) \hat{d}_{ia} e_x^{\text{sl}}(\mathbf{r}_1) + \hat{d}_{ia} g(\mathbf{r}_1) \hat{d}_{jb} e_x^{\text{sl}}(\mathbf{r}_1)] d\mathbf{r}_1 \quad (22)$$

and

$$(ialf_x^{\text{LH}} | bj) = -\frac{1}{2} \int \int [g(\mathbf{r}_1) + g(\mathbf{r}_2)] \frac{\varphi_i^*(\mathbf{r}_1) \varphi_a(\mathbf{r}_2) \varphi_b(\mathbf{r}_1) \varphi_j^*(\mathbf{r}_2)}{|\mathbf{r}_1 - \mathbf{r}_2|} d\mathbf{r}_1 d\mathbf{r}_2 - \frac{1}{2} \int \int \hat{d}_{jb} [g(\mathbf{r}_1) + g(\mathbf{r}_2)] \sum_k \frac{\varphi_i^*(\mathbf{r}_2) \varphi_a(\mathbf{r}_1) \varphi_k^*(\mathbf{r}_1) \varphi_k(\mathbf{r}_2)}{|\mathbf{r}_1 - \mathbf{r}_2|} d\mathbf{r}_1 d\mathbf{r}_2 - \frac{1}{2} \int \int \hat{d}_{ia} [g(\mathbf{r}_1) + g(\mathbf{r}_2)] \sum_k \frac{\varphi_b(\mathbf{r}_1) \varphi_j^*(\mathbf{r}_2) \varphi_k(\mathbf{r}_1) \varphi_k^*(\mathbf{r}_2)}{|\mathbf{r}_1 - \mathbf{r}_2|} d\mathbf{r}_1 d\mathbf{r}_2 - \frac{1}{2} \int \int \hat{d}_{ia} \hat{d}_{jb} g(\mathbf{r}_1) \sum_{kl} \frac{\varphi_k^*(\mathbf{r}_1) \varphi_k(\mathbf{r}_2) \varphi_l(\mathbf{r}_1) \varphi_l^*(\mathbf{r}_2)}{|\mathbf{r}_1 - \mathbf{r}_2|} d\mathbf{r}_1 d\mathbf{r}_2 + \int [\{1 - g(\mathbf{r}_1)\} \hat{d}_{ia} \hat{d}_{jb} e_x^{\text{sl}}(\mathbf{r}_1) - \hat{d}_{ia} \hat{d}_{jb} g(\mathbf{r}_1) e_x^{\text{sl}}(\mathbf{r}_1)] d\mathbf{r}_1 - \int [\hat{d}_{jb} g(\mathbf{r}_1) \hat{d}_{ia} e_x^{\text{sl}}(\mathbf{r}_1) + \hat{d}_{ia} g(\mathbf{r}_1) \hat{d}_{jb} e_x^{\text{sl}}(\mathbf{r}_1)] d\mathbf{r}_1 \quad (23)$$

The concatenation of two semi-local potential operators \hat{d}_{pq} and \hat{d}_{rs} results from differentiation of the LMF with respect to the ground-state density-matrix elements D_{pq} and D_{rs} , thus accounting for all combinations of second partial derivatives with respect to ρ , γ , and τ .

For a constant LMF $g(\mathbf{r}) = c$, the LH kernel integrals 22 and 23 correctly reduce to the well-known global hybrid kernel integrals

$$(ialf_x^{GH}|jb) = -c \iint \frac{\varphi_i^*(\mathbf{r}_1) \varphi_a(\mathbf{r}_2) \varphi_j(\mathbf{r}_1) \varphi_b^*(\mathbf{r}_2)}{|\mathbf{r}_1 - \mathbf{r}_2|} d\mathbf{r}_1 d\mathbf{r}_2 + (1-c) \int \hat{d}_{ia} \hat{d}_{bj} e_x^{sl}(\mathbf{r}_1) d\mathbf{r}_1 \quad (24)$$

$$(ialf_x^{GH}|bj) = -c \iint \frac{\varphi_i^*(\mathbf{r}_1) \varphi_a(\mathbf{r}_2) \varphi_b(\mathbf{r}_1) \varphi_j^*(\mathbf{r}_2)}{|\mathbf{r}_1 - \mathbf{r}_2|} d\mathbf{r}_1 d\mathbf{r}_2 + (1-c) \int \hat{d}_{ia} \hat{d}_{jb} e_x^{sl}(\mathbf{r}_1) d\mathbf{r}_1 \quad (25)$$

As proposed by Furche et al.,⁴¹ in TDDFT the usual kinetic-energy density τ should be replaced by a generalized kinetic-energy density $\tilde{\tau}$ to ensure gauge invariance. Introducing the paramagnetic current density

$$\mathbf{j}(\mathbf{r}) = \frac{1}{2} \sum_{pq} D_{pq} [\nabla \varphi_p^*(\mathbf{r}) \varphi_q(\mathbf{r}) - \varphi_p^*(\mathbf{r}) \nabla \varphi_q(\mathbf{r})] \quad (26)$$

the modified kinetic-energy density is defined as

$$\tilde{\tau}(\mathbf{r}) = \tau(\mathbf{r}) - \frac{1}{2} \frac{\mathbf{j}^2(\mathbf{r})}{\rho(\mathbf{r})} \quad (27)$$

For current-free ground states, i.e., in the absence of a magnetic field or of spin-orbit coupling, the generalized $\tilde{\tau}$ reduces to τ . Furthermore, meta-GGAs and the so-called current-dependent meta-GGAs (cMGGA), which use the generalized $\tilde{\tau}$, give the same potential, whereas additional terms arise in the exchange-correlation kernel due to the response of the current density. In the case of cMGGA, the current-density response reduces to a first derivative with respect to the kinetic-energy density, as shown by Furche et al.⁴¹ It can be included into the LH exchange kernel by extension of the semi-local potential operator (eq 17)

$$\hat{d}_{pq}^{cr} g(\mathbf{r}) = \varphi_p^*(\mathbf{r}) \varphi_q(\mathbf{r}) \frac{\partial g}{\partial \rho}(\mathbf{r}) + 2 \nabla \rho(\mathbf{r}) \cdot \nabla (\varphi_p^*(\mathbf{r}) \varphi_q(\mathbf{r})) \frac{\partial g}{\partial \gamma}(\mathbf{r}) + \frac{1}{2} \nabla \varphi_p^* \cdot \nabla \varphi_q \frac{\partial g}{\partial \tau}(\mathbf{r}) + \frac{1}{2} [\varphi_p^* \nabla \varphi_q - \nabla \varphi_p^* \varphi_q] \cdot \frac{\partial g}{\partial \mathbf{j}}(\mathbf{r}) \quad (28)$$

and leads to nonvanishing contributions to the magnetic orbital-rotation Hessian (eq 9) only. Note that for current-free ground states the electric orbital-rotation Hessians (eq 8) of a meta-GGA and the corresponding cMGGA do not differ.

Using the local hybrid exchange-correlation kernel integrals 22 and 23, the calculation of the matrix-vector products via eq 7, needed in most programs, is straightforward. Before turning to their implementation, some basic principles of semi-numerical integration schemes will be outlined.

2.3. Semi-numerical Integration Schemes. Although analytical integration has been formerly the method of choice for the calculation of exact exchange, semi-numerical schemes exhibit superior scaling with respect to basis-set and system size. They have been applied to exact exchange in global hybrid functionals for self-consistent calculations,^{36,45–47} two-component calculations,⁴⁸ and molecular gradients^{38,45} as well as TDDFT within the TDA.^{37,38}

The semi-numerical integration is a simplification of Friesner's pseudospectral (PS) method.^{37,46,47} In the PS method, the four-center integrals are factorized in a way that the integration can be done in two different spectral representations, in electronic and in real space

$$(\mu\nu|\kappa\lambda) \approx \sum_g Q_{\mu g} A_{\kappa\lambda g} X_{g\nu} \quad (29)$$

where $X_{g\nu}$ is a basis function χ_ν evaluated at a grid point g

$$X_{g\nu} = \chi_\nu(\mathbf{r}_g) \quad (30)$$

The matrix elements of \mathbf{A} , representing two-center electron-repulsion integrals evaluated at a grid point g

$$A_{\kappa\lambda g} = \int \frac{\chi_\kappa(\mathbf{r}') \chi_\lambda(\mathbf{r}')}{|\mathbf{r}_g - \mathbf{r}'|} d\mathbf{r}' \quad (31)$$

are calculated analytically using standard integration techniques.⁴⁹ In the PS method, the transformation matrix \mathbf{Q} is defined as

$$\mathbf{Q} = \mathbf{S}(\mathbf{X}^T \mathbf{w} \mathbf{X})^{-1} \mathbf{X}^T \mathbf{w} \quad (32)$$

with the overlap matrix \mathbf{S}

$$S_{\kappa\lambda} = \int \chi_\kappa(\mathbf{r}) \chi_\lambda(\mathbf{r}) d\mathbf{r} \quad (33)$$

and the grid weight vector \mathbf{w} . Inspection of 29 shows that the PS method scales linearly with the number of grid points n . The evaluation of \mathbf{A} for one grid point depends quadratically on the number of basis functions N_{BF} . The multiplication with a density matrix also scales with N_{BF}^2 for every grid point. Hence, the PS method exhibits formally a cubic scaling with respect to system size.

As already pointed out by Friesner,³⁷ the PS method is closely related to a pure semi-numerical integration scheme. Assuming

$$\mathbf{Q} = \mathbf{X}^T \mathbf{w} \quad (34)$$

for the transformation matrix in 29 leads to the semi-numerical integration scheme

$$(\mu\nu|\kappa\lambda) \approx \sum_g w_g \cdot X_{g\mu} X_{g\nu} A_{\kappa\lambda g} \quad (35)$$

As for the PS method, the calculation cost formally scales with $n \cdot N_{\text{BF}}^2$.

In the COSX approximation, concepts similar to linear-scaling analytical integral evaluation techniques, such as the LinK method,⁵⁰ are combined with the semi-numerical integration scheme to obtain a linear-scaling algorithm for the calculation of exact exchange.⁴⁵ The exact-exchange matrix, needed in ground-state calculations, is computed by contracting four-center integrals with the density matrix \mathbf{D}

$$K_{\mu\nu} = \sum_{\kappa\lambda} D_{\mu\lambda} (\mu\nu|\kappa\lambda) \approx \sum_g \sum_{\kappa\lambda} w_g \cdot X_{g\nu} A_{\kappa\lambda g} D_{\mu\lambda} X_{g\mu} \quad (36)$$

where the density matrix is defined as usually in the AO basis as a sum over molecular-orbital coefficients $C_{k\mu}$

$$D_{\mu\nu} = \sum_k C_{k\mu} C_{k\nu} \quad (37)$$

The central tool for the efficiency of COSX are S- and P-junctions.^{45,51} The first refers to prescreening of \mathbf{A} -matrix

elements by considering the overlap of entire shells (basis functions with the same l quantum number). Additionally, analytical integrals $A_{\kappa\lambda g}$ can be neglected if the shells are not connected to the contributing basis functions on a given batch of grid points via density-matrix elements. Substeps in the calculation of 36 are contraction of the basis-function vector with the density matrix and the square root of the grid-point vector

$$F_{\kappa g} = \sum_{\lambda} \sqrt{w_g} \cdot D_{\kappa\lambda} X_{\lambda g} \quad (38)$$

followed by evaluation of the product

$$G_{\mu g} = A_{\mu\kappa g} F_{\kappa g} \quad (39)$$

and subsequently taking the sum over grid points

$$K_{\mu\nu} = \sum_g \sqrt{w_g} \cdot G_{\mu g} X_{g\nu} \quad (40)$$

This procedure efficiently reduces the number of analytical integrals to be calculated on each grid point, eventually leading to linear scaling as the number of non-negligible density-matrix elements becomes independent of the basis-set size. A more detailed description can be found in refs 45 and 51.

For the Coulomb interaction, a pure semi-numerical scheme without dealiasing functions and other features of the PS method may lead to numerical instabilities. This is due to the more long-ranged character of Coulomb compared to exchange contributions, as has been pointed out by van Wüllen.⁵² We encountered convergence problems in the present implementation when applying the semi-numerical integration also to the Coulomb contributions. van Wüllen has solved these issues by introducing a model electron density of s-character on every atom, for which analytical integrals can be easily calculated. The additional basis functions can be related to the dealiasing functions used in the more sophisticated ansatz for the transformation matrix \mathbf{Q} in the PS method, which does not seem to suffer from these problems. Yet, in a pure semi-numerical integration scheme, inclusion of the Coulomb integrals is not recommended.

To circumvent the bottleneck of four-center analytical Coulomb integrals nonetheless, semi-numerical exact exchange is best combined with the RI-J approximation,^{53–56} as already pointed out and used by Neese and co-workers.^{45,51} The resulting combined integration scheme scales as $n \cdot N_{\text{BF}}^2$ for the exchange part and as $N_{\text{aux}} \cdot N_{\text{BF}}^2$ (with N_{aux} being the number of auxiliary basis functions) for the Coulomb part. Both the RI-J and the COSX method are well-established in TDDFT calculations.^{38,56} They have been used in an efficient self-consistent implementation of local hybrid functionals.³⁶ We have employed this combination here for the efficient implementation of local hybrid functionals into linear response TDDFT. To our knowledge, such an RIJ-COSX scheme so far has been presented only for global hybrid functionals and only within the Tamm–Dancoff approximation. Its efficiency and accuracy for global hybrids are, therefore, assessed here as well.

2.4. The Semi-numerical Scheme in TDDFT with Local Hybrids. To illustrate the semi-numerical approach for the implementation of hybrid functionals, and in particular LHs, for TDDFT, the kernel integrals are projected into the atomic-orbital basis, and the final matrix–vector products defined in eq 7 are outlined below. For simplicity, complex notations are dropped, assuming that all orbitals are real, and only matrix

elements that originate from exact-exchange related quantities are shown. The semi-local terms are not inserted into the semi-numerical scheme. They can be calculated efficiently based on the existing implementation of TDDFT in TURBOMOLE.

For clarity, we again suppress spin indices, assuming separated spin channels for the exchange part. Exchange matrix–vector products for closed-shell ground states thus become the same for singlet and triplet excitations. Extension to functionals that violate the spin-channel separation, as is the case for common LMFs,³⁴ is straightforward when the semi-local potential operators are replaced by their spin-resolved counterparts. Singlet and triplet matrix–vector products then become different.

As pointed out in the previous section, the integration over DFT quantities is usually performed on a numerical grid. The matrix–vector products \mathbf{V}^{\pm} are then expressed as a sum over matrix–vector products \mathbf{V}_g^{\pm} computed at each grid point and weighted by the grid-weight factor w_g

$$\mathbf{V}^{\pm} = \sum_g w_g \cdot \mathbf{V}_g^{\pm} \quad (41)$$

For brevity, the grid-point index will be suppressed in the following formulas. The ground-state density matrix is denoted \mathbf{D} (see eq 37). To avoid confusion with the basis-function vector \mathbf{X} (see eq 30), the symmetric and antisymmetric parts of the transition-density matrices $(\mathbf{X} \pm \mathbf{Y})$ are relabeled as

$$P_{\mu\nu} = (\mathbf{X} + \mathbf{Y})_{\mu\nu} \quad (42)$$

$$U_{\mu\nu} = (\mathbf{X} - \mathbf{Y})_{\mu\nu} \quad (43)$$

For local hybrids, the exact-exchange contributions to the symmetric matrix–vector product on each grid point are given in terms of the density matrices, and the \mathbf{A} -matrix (cf. eq 31), by

$$\begin{aligned} \mathbf{V}(\text{exx})_{\mu\nu}^+ &= -g[X_{\mu}(\mathbf{A}\mathbf{P}\mathbf{X})_{\nu} + (\mathbf{A}\mathbf{P}\mathbf{X})_{\mu}X_{\nu}] \\ &\quad - \sum_{\kappa\lambda} P_{\kappa\lambda} \hat{d}_{\kappa\lambda g} [X_{\mu}(\mathbf{A}\mathbf{D}\mathbf{X})_{\nu} + (\mathbf{A}\mathbf{D}\mathbf{X})_{\mu}X_{\nu}] \\ &\quad - 2 \cdot \hat{d}_{\mu\nu g} (\mathbf{X}^T \mathbf{D} \mathbf{A} \mathbf{P} \mathbf{X}) - \sum_{\kappa\lambda} P_{\kappa\lambda} \hat{d}_{\mu\nu} \hat{d}_{\kappa\lambda g} (\mathbf{X}^T \mathbf{D} \mathbf{A} \mathbf{D} \mathbf{X}) \end{aligned} \quad (44)$$

Note that the molecular orbitals in the semi-local potential operators \hat{d}_{pq} (cf. eq 17) are now replaced by atomic orbitals. The exact-exchange based contributions to the antisymmetric matrix–vector product are

$$\mathbf{V}(\text{exx})_{\mu\nu}^- = -g[X_{\mu}(\mathbf{A}\mathbf{U}\mathbf{X})_{\nu} - (\mathbf{A}\mathbf{U}\mathbf{X})_{\mu}X_{\nu}] \quad (45)$$

For global hybrid functionals, i.e., a constant LMF, only the first line of 44 remains, and the exact-exchange contributions to the antisymmetric matrix–vector product are the same for local and global hybrids. As pointed out above, an additional kernel term appears if the current-density response is considered for LMFs that depend on the kinetic-energy density. While these terms vanish in the symmetric matrix–vector product, the exact-exchange contribution to the antisymmetric matrix–vector product becomes

$$\begin{aligned} \mathbf{V}(\text{exx, cdr})_{\mu\nu}^- &= -g[X_{\mu}(\mathbf{A}\mathbf{U}\mathbf{X})_{\nu} - (\mathbf{A}\mathbf{U}\mathbf{X})_{\mu}X_{\nu}] \\ &\quad - \frac{1}{4} (X_{\mu} \nabla X_{\nu} - \nabla X_{\mu} X_{\nu}) \frac{1}{\rho} \frac{\partial g}{\partial \tau} (\mathbf{X}^T \mathbf{U} \nabla \mathbf{X} - \nabla (\mathbf{X}^T) \mathbf{U} \mathbf{X}) \\ &\quad (\mathbf{X}^T \mathbf{D} \mathbf{A} \mathbf{D} \mathbf{X}) \end{aligned} \quad (46)$$

when the corresponding semi-local potential operator defined in eq 28 is used instead of eq 17. For later use, only nonlocal terms that are not fully contracted with density matrices are referred to as nonlocal contributions to the matrix–vector products, i.e., the first two lines in eq 44 as well as the first line in eqs 45 and 46. Hence, the remaining terms in these equations result only in semi-local contributions while containing nonlocal quantities like the exact-exchange energy density.

From eqs 44–46, it is apparent that the P-junctions for prescreening of the A-matrix elements have to be extended to the symmetric and antisymmetric parts **P** and **U** of the transition-density matrices, respectively: In the spirit of the semi-numerical scheme, a stepwise procedure is applied. First, the basis-function vector with *k* contributing basis functions on a batch of grid points is contracted with the ground-state and the symmetric and antisymmetric transition-density matrices for each excitation *i*

$$\begin{aligned} F_{\mu} &= \sum_{\lambda}^k D_{\mu\lambda} X_{\lambda} \\ F_{\mu}^{i,+} &= \sum_{\lambda}^k P_{\mu\lambda}^i X_{\lambda} \\ F_{\mu}^{i,-} &= \sum_{\lambda}^k U_{\mu\lambda}^i X_{\lambda} \end{aligned} \quad (47)$$

The resulting F-matrices are subsequently multiplied with the precalculated A-matrices (cf. eq 31) defining the intermediate G-matrices

$$\begin{aligned} G_{\mu} &= \sum_{\kappa} A_{\mu\kappa} F_{\kappa} \\ G_{\mu}^{i,+} &= \sum_{\kappa} A_{\mu\kappa} F_{\kappa}^{i,+} \\ G_{\mu}^{i,-} &= \sum_{\kappa} A_{\mu\kappa} F_{\kappa}^{i,-} \end{aligned} \quad (48)$$

The exact-exchange part of the matrix–vector products per grid point defined in eqs 44–46 is subsequently assembled from the matrices **F** and **G** and the basis-function vector **X**. The grid weights are included in the last step, where the final matrix–vector products are calculated through eq 41.

In the following section, the general implementation, the prescreening procedure, and the related matrix multiplications for an efficient TDDFT calculation with local and global hybrid functionals will be explained in detail.

3. IMPLEMENTATION

We implemented the local hybrid exchange-correlation kernel into a development version of the TURBOMOLE program package, making use of existing algorithms to solve the TDDFT equations⁶ and routines for the evaluation of analytical as well as RI-J Coulomb integrals.^{54,56}

The implementation of eqs 44–46 is conveniently separated into several steps with the intermediate vectors **F**, **F**^{*i*±}, **G**, and **G**^{*i*±} defined in eqs 47 and 48. These steps have to be executed for every grid point, arranged into grid-point batches to reduce memory requirements. In addition, in TDDFT some steps have to be repeated for every excitation. Figure 1 shows the

complete sequence of steps for the calculation of the local hybrid exchange-correlation matrix–vector products.

– Determine S-junctions	N_{BF}^2
▷ Loop over grid points:	
– Evaluate basis-function vector X	N_{BF}
– Determine P-junctions	N_{BF}^2
– Perform matrix-vector multiplication F = DX	N_{BF}^2
– Determine ground-state quantities ρ, γ, τ	N_{BF}
– Determine functional and LMF derivatives	1
– Calculate matrix A	N_{BF}^2
– Perform matrix-vector multiplication G = AF	N_{BF}^2
▷ Loop over <i>i</i> excitations:	
– Perform matrix-vector multiplication F ^{<i>i</i>+} = P ^{<i>i</i>} X	N_{BF}^2
– Determine transition-state quantity $\nabla\rho^i$	N_{BF}
– Perform matrix-vector multiplication F ^{<i>i</i>−} = U ^{<i>i</i>} X	N_{BF}^2
– Determine transition-state quantity j ^{<i>i</i>}	N_{BF}
– Perform matrix-vector multiplication G ^{<i>i</i>+/−} = AF ^{<i>i</i>,sy/as}	N_{BF}^2
– Calculate non-local parts of the kernel	N_{BF}
– Calculate semi-local parts of the kernel	1
– Build non-local part of matrix-vector product V _g [±]	N_{BF}^2
– Build semi-local part of matrix-vector product V _g [±]	N_{BF}^2

Figure 1. Steps and their formal scaling in the semi-numerical calculation of local hybrid exchange-correlation kernel integrals (closed-shell case). Indices for grid points are omitted. **D**, **P**, and **U** denote density matrices (ground and excited state), **F**, contracted density matrices, and **G**, their contraction with matrix **A** (see Section 2.3). Semi-local and nonlocal parts in the sense of matrix–vector products are defined in Section 2.3.

S-junctions are computed and used to prescreen off-diagonal elements of **A** in the same fashion as for ground-state DFT. They are calculated only once per TDDFT calculation before the grid iteration. More details can be found in refs 36 and 45. P-junctions are determined after evaluating the basis-function vector **X**. Their implementation for TDDFT will be discussed further below.

In TDDFT calculations with semi-local functionals, multiplication of the ground-state density matrix **D** with the basis-function vector is needed only to determine the ground-state density, its derivatives, and the kinetic energy density. If a reduced number of basis functions *k* contributes to a batch of grid points, then a quadratic submatrix with dimension *k* × *k* of **D** is required. In a local hybrid calculation, the product **F** (eq 47) is further used for nonlocal contributions of the exchange-correlation kernel. Hence, the complete vector is needed, rather than only *k* elements. Further below, we will discuss how the sparsity of **X** can be used to circumvent multiplication with the complete density matrix and how this scheme can be transferred to other matrix–vector multiplications, such as the multiplication of **A** with **F**. The latter is exclusively needed by local hybrid functionals, because global hybrid functionals do not include exact-exchange potential-like terms.

In ground-state DFT calculations, the **A** matrix is calculated and immediately contracted with the F-matrix (see ref 36). Due to the fact that in TDDFT two additional transition-density matrices per excitation have to be multiplied with **A**, it is more efficient to precalculate and store the entire matrix explicitly.

All of the steps mentioned above are independent of the number of excitations and are computed before the excitation loop. In the limit of an infinite number of excitations, the cost for calculating **A**, **F**, and **G** is negligible compared to the

calculation of their counterparts for the transition-density matrices. This contrasts with ground-state calculations, where computation of **A** and **G** is by far the most time-consuming part. Hence, an efficient calculation of $F^{i\pm}$ and $G^{i\pm}$ becomes more important for TDDFT and will be discussed in detail further below. Besides the above-mentioned matrix–vector multiplication, the exchange–correlation matrix–vector product has to be calculated separately for each excitation. This includes the semi- and nonlocal parts as well as the symmetric and antisymmetric parts of the matrix–vector product.

Formally, the complete algorithm scales linearly with the number of grid points n , inherent to the grid integration, and quadratically with the number of basis functions N_{BF} . The formal scaling of each separate step is shown in Figure 1. The importance of the individual scaling behavior of different terms is regulated by the prefactor. That is, the evaluation of **X**, the determination of the DFT quantities, the calculation of the non- and semi-local parts of the kernel, and the evaluation of functional derivatives will not dominate the calculation even for large systems. Hence, we will not consider these steps in our further discussion of the efficiency of our implementation. Both the calculation of the matrix **A**, considering S- and P-junctions, and the optimization of the crucial linear-algebra operations will be discussed next.

3.1. P-Junctions for Hybrids in TDDFT. For TDDFT, a variation of the procedure introduced previously for the ground state has to be applied, since, additionally, transition-density matrices have to be taken into account. Overall, $1 + 2 \cdot i$ density matrices are screened, where i is the number of excited states considered. Since the products of the transition-density matrices and the basis-function vector, which are needed to determine P-junctions, are calculated after the computation of the **A** matrix, approximations have to be introduced.

The first one concerns the basis-function vector. Instead of using it explicitly for every grid point, a vector with the maximum basis-function values for the current grid batch is utilized. For a moderate amount of excitations, this vector can be multiplied with all density matrices separately to use the resulting vectors for the determination of the P-junctions. The second approximation affects the density matrices themselves. On the basis of all density matrices, a temporary matrix can be constructed, which consists of the maximum absolute values of all density matrices. This matrix is then multiplied with the maximum absolute basis function vector to determine the P-junctions. To ensure that only one matrix–vector multiplication has to be performed, a density-matrix screening has to be done. While this screening has a small prefactor, making it less time determining, it scales quadratically. In addition, the accuracy of the estimated P-junctions is slightly decreased. Large numbers of excitations are thus accessible without sacrificing efficiency. Overall, both variants for approximated P-junctions scale as N_{BF} and by construction cannot result in false unjunctioned shells.

Besides the obstacles in the implementation, the efficiency of P-junctions for TDDFT calculations in general is arguable. Due to the larger number of density matrices, more shells and thus more basis functions are junctioned. In the limit of a complete set of single excitations, all shells are junctioned with each other. In practice, rarely more than a few low-lying excitations are needed so that P-junctions might play a role. We will show further below that for up to medium-sized alkene chains this is not the case. Nevertheless, the computational cost for the determination of P-junctions within one of the presented

approximations may be neglected in comparison to the other algebraic steps. Furthermore, the vector computed to determine the P-junctions can be used to accelerate the following matrix–vector multiplications.

3.2. Optimized Algebra Routines. Besides calculation of the **A** matrix, the algebraic operations, especially the multiplication of **F** with the **A** matrix, are the most time-consuming steps. The first of them is the multiplication of density matrices with the basis function vector **X**. Formally, this step scales as N_{BF}^2 . Due to the sparsity of **X**, only rectangular density matrices with dimensions $k \times N_{\text{BF}}$ have to be used, with k being the number of contributing basis functions in **X**. Additionally, the symmetry of the density matrices can be utilized. The rectangular matrix thus decomposes into an (anti)symmetric quadratic matrix with dimensions $k \times k$ and a remaining rectangular $k \times (N_{\text{BF}} - k)$ matrix. In case of symmetric density matrices, the former submatrix can be treated with symmetric BLAS routines, whereas for antisymmetric matrices, the use of BLAS routines for general matrices gives more benefits than manual multiplication using antisymmetry. The dimension of the latter submatrix can be further reduced by utilizing the temporary vector calculated for the determination of the P-junctions. Recall that this vector is a conservative approximation to the maximum absolute values of **F**. Therefore, it is screened for nonzero elements (denoted here as m), and only these have to be considered in the rectangular submatrix. Applying both symmetry and prescreening, the matrix multiplication scales as $\frac{1}{2}k^2 + \left(m + \frac{1}{2}\right)k$. Using only the prescreening in the antisymmetric cases results in a scaling of $k^2 + mk$. Both scalings are independent of N_{BF} , as required for an overall linear scaling. Nevertheless, as discussed in the context of P-junctions, the overall efficiency strongly depends on the nature of the density matrices and the number of excitations.

The next algebraic step involves the symmetric **A** matrix and the vector **F**. In contrast to density matrices, **A** depends on the grid coordinate, and the matrix–vector multiplication in eq 48 has to be carried out separately at each grid point. In contrast to the multiplication of density matrices, only BLAS level 2 routines could be used for this algebraic operation, which, in comparison to BLAS level 3 routines, provide less acceleration. Nevertheless, in general, all considerations made for symmetric density matrices can also be applied to **A**. First, the vectors **F** for a grid batch are screened for nonzero elements, allowing the described separation of the **A** matrix into a quadratic and a rectangular part to be performed. As a second step, the rectangular part of the **A** matrix is screened for nonzero rows. While the prescreenings scale linearly, the matrix multiplication itself, which is the time-determining step, formally does not scale with the system size, even though this also depends strongly on the effectiveness of the P-junctions.

The last algebraic step is the formation of the matrix–vector products. As in usual DFT calculations, the semi-local part scales at least as $\frac{1}{2}k^2 + \frac{1}{2}k$ due to the sparsity of the basis-function vector. The nonlocal part can also benefit from a reduced **X** vector. An additional linear prescreening of **G** for nonzero elements then leads formally to an asymptotic linear scaling.

Except for the prescreenings, which are distinguished by a small prefactor and a linear scaling with N_{BF} , all described routines formally do not scale with system size. In combination with S- and P-junctions for the calculation of the **A** matrix, this leads to a formal linear scaling of the overall method. Even if

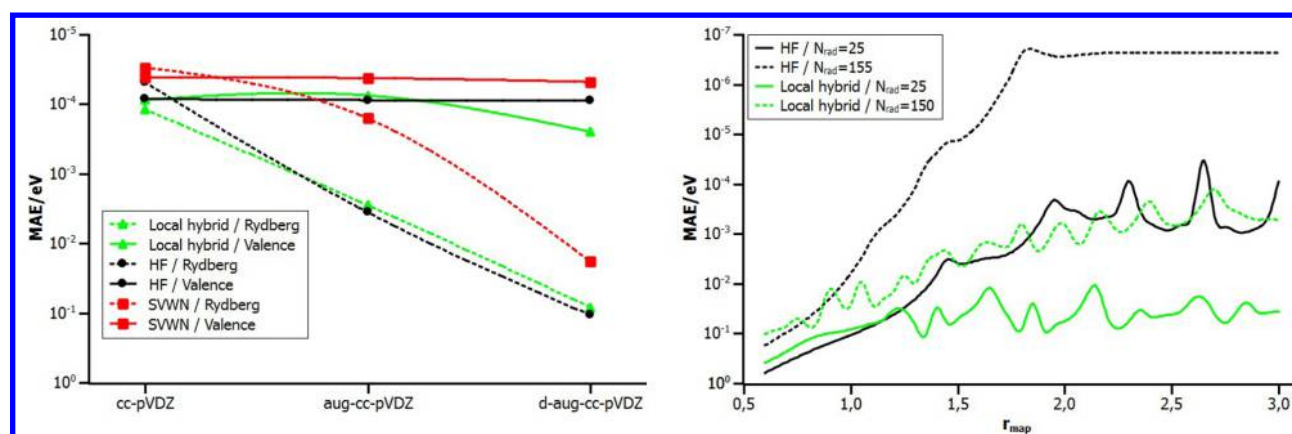


Figure 2. (a) Deviations from reference energy values for the low-lying valence and Rydberg excitations of CO for different basis sets. The small grid (TURBOMOLE grid 1) and a mapping parameter of 1.0 are applied. (b) Dependence on the radial mapping parameter r_{map} of the deviations for low-lying CO Rydberg excitation energies from reference values, calculated with the d-aug-cc-pVDZ basis set and a 1202 point Lebedev grid.

the assumption of linearity for the density matrices does not hold true, the complete algorithm scales as $n \cdot N_{\text{BF}}$ or less in the asymptotic limit.

4. COMPUTATIONAL DETAILS

For the detailed analysis of the accuracy of the new implementation (see Section 5), we utilized the unscaled t-LMF in combination with Slater–Dirac exchange and VWN correlation^{32,57}

$$g_{\sigma} = \frac{\tau_{W,\sigma}}{\tau_{\sigma}} = \frac{1}{8} \frac{\gamma_{\sigma\sigma}}{\rho_{\sigma} \tau_{\sigma}} \quad (49)$$

Besides the errors caused by the integration grid, we investigated interdependencies between the basis set and the excitation type, i.e., for Rydberg and valence excitations.

For the analysis of the integration grid, we employed the commonly used Lebedev and Chebyshev grids for the angular and radial parts, respectively. The radial mapping function M4 from ref 58 is employed, with a variable linear prefactor. In contrast to the previous grid parameters, the partitioning function is kept fixed, i.e., in the form proposed by Becke.⁵⁹ A detailed explanation of the construction of molecular numerical integration grids is given by Ahlrichs and co-workers.⁵⁸ The 110 point Lebedev and 25 point Chebyshev grid is referred to as small grid (TURBOMOLE grid 1).

As a test case for the analysis, we used the seven lowest-lying excitations of the CO molecule, i.e., three valence and four Rydberg excitations. The structure of CO is taken from ref 15 (C–O distance 1.128 Å). Analytical TDHF results serve as reference for semi-numerical TDHF calculations, whereas for SVWN and the local hybrid functional, the reference value is determined using a sufficiently large integration grid (1202 point Lebedev grid, 500 point Chebyshev grid, radial mapping parameter of 3.0). Results are converged to $10^{-10} h$. The mean absolute deviation in electron volts between the reference and the semi-numerical results represents the accuracy. A deviation of 0.01 eV is regarded as target accuracy determined solely by the integration grid, although slightly larger deviations are still acceptable for many purposes. Nevertheless, this conservative bound is consistent with the desired enhanced target accuracy of local hybrid functionals in comparison to experimental and theoretical reference values.⁶⁰

The influence of the basis set is analyzed using the series of Dunning's correlation consistent basis sets,^{61,62} with and

without diffuse basis functions. While different parent sizes (determined by ζ) do not affect the results qualitatively, the addition of diffuse basis functions changes the results significantly. Hence, double- ζ -derived basis sets suffice for the technical investigations.

S- and P-junctions are analyzed using the decapentaene molecule in all-trans conformation. The energy of the lowest-lying valence excitation (1B_u) has been calculated with the def2-TZVP basis set and the small grid (TURBOMOLE grid 1, nondiffuse). As reference, we took very low thresholds of 10^{-100} au for both S- and P-junctions.

To investigate the efficiency and scaling behavior of the new implementation (see Section 6), we compared the existing analytical TURBOMOLE implementation⁶ with the new semi-numerical implementation in combination with RI-J using the TPSSH hybrid functional. Additionally, a local hybrid functional with a scaled t-LMF (prefactor of 0.48⁵⁷) in combination with Slater–Dirac exchange and VWN correlation is used to evaluate any overhead arising in the semi-numerical scheme for local compared to global hybrids. Since timings are evaluated only for valence excitations, a nondiffuse grid was used together with 10^{-6} au thresholds for S- and P-junctions. Timings were measured on an Intel core i7-3770K processor.

5. ACCURACY

In the present implementation, the accuracy of local hybrid excitation energies is determined by the semi-numerical integration scheme and thus by the numerical integration grid.

Figure 2 shows the dependence of the numerical accuracy of Rydberg and valence excitations with respect to the basis-set augmentation using the small grid. While cc-pVDZ results show small deviations for all excitations, augmentation increases the deviations for Rydberg excitations, in particular for TDHF and the local hybrid functional. Deviations of around 0.1 eV from the reference data for the doubly augmented basis are 1 order of magnitude above the target. In contrast, for this basis, SVWN exhibits an error of 0.02 eV. Since augmented basis sets are needed especially for the description of Rydberg excitations, the larger deviations for HF and local hybrid results with the chosen grids are investigated further.

Within the semi-numerical scheme, it is obviously important to account for the additional space spanned by diffuse basis functions by using larger grids. We first analyzed the effect of the radial grid. For this purpose, the angular grid is set to a large

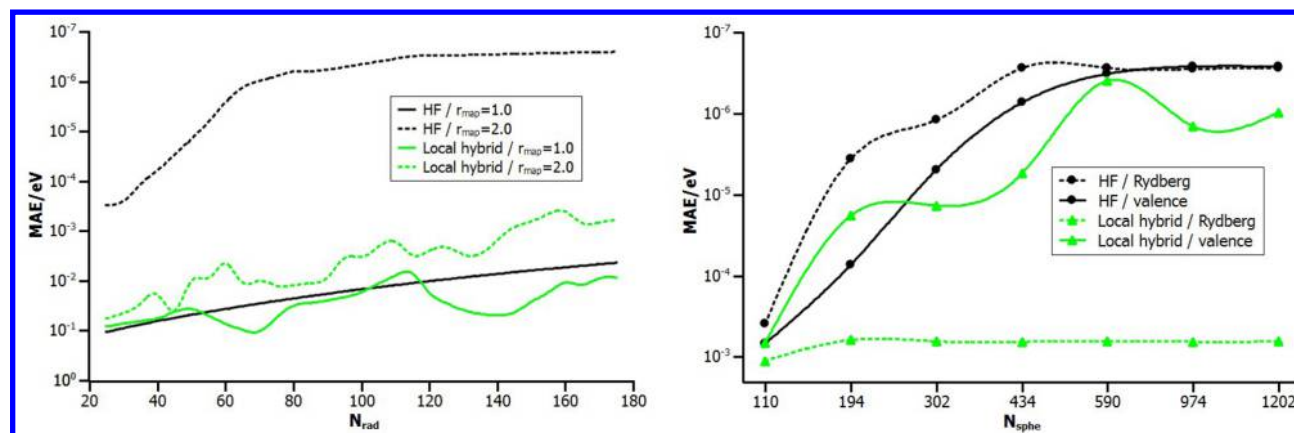


Figure 3. (a) Dependence of the accuracy of the energies of the low-lying Rydberg excitations for CO, calculated with the d-aug-cc-pVDZ basis set and a 1202 point Lebedev grid, on the number of radial grid points N_{rad} . (b) Accuracy of the energies of the low-lying valence and Rydberg excitations for CO depending on the spherical grid size. A 150 point Chebyshev grid, a mapping parameter of 2.0, and the d-aug-cc-pVDZ basis set are applied.

1202 point Lebedev grid. The variation of the relative radial mapping parameter r_{map} shifts the center of radial grid points. Values larger than 1.0 give more diffuse grids, whereas smaller values result in a contracted grid. Results for an overall small and large radial grid size are shown in Figure 2. In general, the accuracy increases for more diffuse grids. For semi-numerical TDHF, the target accuracy is reached with a mapping parameter of 1.4, even with the small radial grid. The standard parameter of 1.0 is already sufficient to reach the target accuracy; full convergence is obtained for values larger than 2.0. Even by maximizing the mapping parameter, the target accuracy cannot be reached with the smaller grid (1202 point Lebedev, 25 point Chebyshev grid) for the local hybrid functional. Using the larger radial grid (155 point Chebyshev grid), a mapping parameter of about 1.5 is required to obtain accurate results. Both local hybrid curves exhibit oscillations. Although this effect is also observed for the TDHF results with the smaller grid, it is more pronounced for local hybrids. Most probably, the larger sensitivity of the local hybrid results to grid diffuseness compared to TDHF is due to the form of the local hybrid, where the errors are determined by the product of LMF and EXX energy density. Consequently, a more balanced grid is required that accounts for the local exact-exchange admixture inside the molecule and covers the additional space spanned by the diffuse basis functions. In addition to the mapping parameter, a dependence on the number of radial grid points N_{rad} is observed. This is illustrated for a default and diffuse grids ($r_{\text{map}} = 1.0$ and 2.0) in Figure 3. In combination with the small mapping parameter, TDHF needs about 125 radial grid points to reach an accuracy of 0.01 eV. The local hybrid could not satisfy this criterion with the default grid, whereas with the diffuse grid, it is reached with 55 radial grid points.

Analysis of the dependence of excitation energies on the angular grid size is performed with a large and diffuse grids ($r_{\text{map}} = 2.0$ and 150 radial points) to ensure an accuracy of at least 0.01 eV. The screening of seven different Lebedev grids for Rydberg and valence excitations is shown in Figure 3. For TDHF, the accuracy for Rydberg and valence excitations increases with the number of angular grid points. This holds also for valence excitations with the local hybrid functional. The accuracy for Rydberg excitations, on the other hand, is not affected by an increased spherical-grid size. Most probably, their accuracy is limited by regions with steep transitions between

local and exact exchange, which, in the case of Rydberg excitations, mainly occur in the radial distribution. Hence, Rydberg excitations do not benefit from an increased spherical grid.

The example of the CO molecule shows that small angular and radial grids already give a satisfying accuracy for local hybrid calculations of valence excitations, whereas Rydberg excitations require modifications of the radial grid when diffuse basis sets are used. Besides a moderate augmentation of the number of radial grid points, the use of diffuse grids, i.e., an increased relative radial mapping parameter, is inherently needed to reach a target accuracy beyond 0.01 eV. That is, diffuse states require diffuse basis functions and diffuse grids. For Rydberg excitations, the relative radial mapping parameter and the number of radial grid points thus should be increased at least by a factor of 2.0 and by 20 grid points, respectively. While semi-numerical TDHF is less sensitive than local hybrid functionals, overall comparable behavior could be observed. Previous studies using the pseudospectral method³⁷ or the RIJ-COSX method³⁸ may also have been influenced by the choice of grids.

The S- and P-junctions influence the efficiency of the calculation but might also limit the accuracy of the local hybrid calculations. Therefore, we evaluated the errors introduced by both approximations, with thresholds ranging from 10^{-3} to 10^{-10} au. Use of S-junctions gave stable TDDFT results in the entire range. From 10^{-6} to 10^{-10} au, similar deviations of only ca. 10^{-5} eV are obtained. Nevertheless, already with these moderate thresholds, around one-third of the shell pairs of the **A** matrix could be neglected, leading to substantial computational savings. Looser thresholds resulted in deviations of up to 10^{-3} eV, but they allow almost half of the **A** matrix shell pairs to be neglected.

P-junctions affected the calculation only for thresholds looser than 10^{-7} au; otherwise, no shell pair was neglected for any grid-point batch. Thresholds of 10^{-6} and 10^{-5} au gave stable results with insignificant deviations from the reference values. However, averaging over the entire grid, less than one shell pair was neglected. Still looser thresholds resulted in nonconverging TDDFT calculations. Hence, P-junctions do not play an important role for the semi-numerical TDDFT scheme. Even for larger molecules, such as the linear C_{20} alkene chain, only a minor effect of P-junctions could be found.

6. TIMINGS

The efficiency of the new implementation with respect to system size is studied using the lowest-lying excitation of conjugated polyene chains (in all-trans conformation) with the molecular formula $C_{2i}H_{2i+2}$ ($i = 1-10$). In contrast to bulkier molecules, polyene chains allow maximal time savings due to nonoverlapping basis functions. Hence, the analytical algorithm should benefit more than the semi-numerical one due to the evaluation of four-center rather than only two-center integrals. Linear growth of the integration grid with respect to system size is unavoidable, so polyene chains represent the worst case for a comparison with an analytical implementation. In addition, the medium-sized def2-TZVP basis used does not yet favor the semi-numerical scheme due to the scaling properties of the semi-numerical scheme (cf. Section 3). The CPU times per TDDFT iteration t are shown in Figure 4. Ethene and

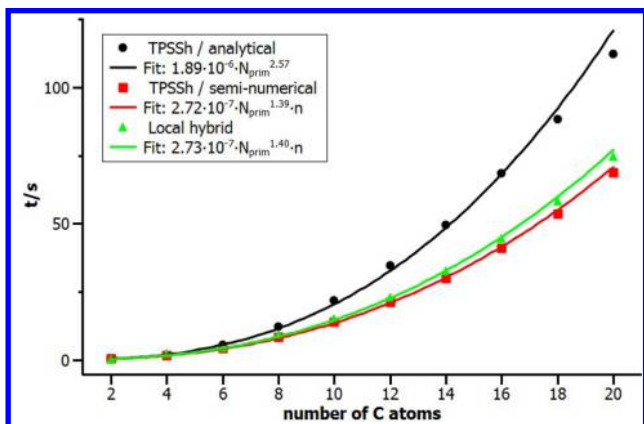


Figure 4. Scaling of the computation time per TDDFT iteration t with respect to number of C atoms in polyene chains with increasing length using the def2-TZVP basis. The fits with respect to the number of primitive basis functions N_{prim} are done for logarithmic scales.

butadiene were neglected for the fit of the scaling behavior due to the large relative errors for small t values. For all molecules larger than butadiene, the semi-numerical implementation is faster than the analytical one. Additionally, the scaling is also somewhat better. Larger basis sets or nonlinear molecules further increase the efficiency of the semi-numerical algorithm in comparison to the analytical implementation due to the scaling properties and the less importance of the overlap screening (cf. Section 3). The systems studied are too small to allow us to judge if the semi-numerical implementation could reach linear or subquadratic scaling for large molecules, but this has not been the goal of the present work.

To evaluate the efficiency with respect to basis-set size, we used the lowest-lying excitation of ethene. Dunning's cc-pVXZ, aug-cc-pVXZ, and d-aug-cc-pVXZ ($X = D, T, Q, 5$) basis sets as well as the TURBOMOLE def2-basis sets, i.e., SVP, SVPD, TZVP, TZVPP, TZVPD, TZVPPD, QZVP, and QZVPD, are employed. Increasing basis-set size should favor the semi-numerical algorithm, since formally only a quadratic scaling is expected, in contrast to the formal quartic scaling of the analytical implementation. Results are shown in Figure 5. The semi-numerical implementation has only half the scaling of the analytical algorithm. Quadratic scaling could not be reached due to the additional scaling of the integral evaluation with respect to orbital angular-momentum quantum number, i.e., l^5

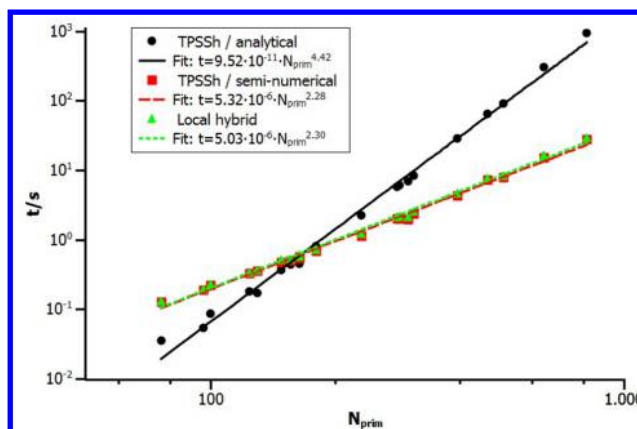


Figure 5. Scaling of the computation time per TDDFT iteration t with respect to number of primitive basis functions N_{prim} for the ethene molecule using different basis sets, Dunning's (d-aug-)cc-pVXZ ($X = D, T, Q, 5$) basis sets, and Ahlrichs' def2 basis sets.

for the two-center and l^{10} for the four-center integrals. S- and P-junctions are not effective for the ethene molecule.

In both comparisons, the semi-numerical treatment is only slightly faster for the global hybrid than for the local hybrid due to the additional terms arising in the local hybrid kernel. However, compared to the overall computational cost, the differences are essentially negligible. Overall, the cost for TDDFT calculations with local hybrid functionals is almost equal to semi-numerical global hybrid calculations, which, in turn, are substantially more efficient than the analytical implementation.

7. EXCITATION ENERGIES FOR FREE-BASE PORPHYRIN

To demonstrate the applicability of TDDFT with local hybrid functionals to larger molecules, we calculated the lowest-lying excitation energies of a well-studied biomolecule, free-base porphyrin. We used the same local hybrid functional⁵⁷ discussed in Section 6 and compared results with the B3LYP global hybrid functional.⁶³ The structure is taken from the work of Perun et al.⁶⁴ Jensen's aug-pc-X ($X = 0, 1, 2, 3$) basis sets⁶⁵⁻⁶⁷ were used to evaluate convergence of the excitation energies with a systematic increase of basis-set size. As shown above, the new semi-numerical implementation exhibits good scaling with respect to basis-set size, enabling the use of large basis sets for larger molecules.

Table 1 compares the results to experimental values.⁶⁸ For the 12 calculated lowest-lying excitations, the local hybrid functional gives similar excitation energies as those with B3LYP. Since these are mainly valence excitations, this shows the general validity of the chosen simple local hybrid. On the other hand, results for the $2B_{2g}$ excitation differ by more than 0.7 eV, suggesting that there are notable differences between the two functionals. We postpone a detailed analysis of the general performance of local hybrids to a separate publication, where a larger variety of LMFs will be evaluated systematically. This should, of course, also include more difficult excitation types to see if local hybrids indeed provide advantages over other functionals. We note in passing that LMFs can be constructed in various ways, either based on physical considerations but involving semiempirical parametrization or based on first-principles, e.g., using a local version of the adiabatic connection.⁶⁹

Table 1. Basis-Set Dependence of Excitation Energies of Free-Base Porphyrin (in eV) for B3LYP and a Simple Local Hybrid Functional^a

state	B3LYP				local hybrid				exp. ^b
	aug-pc-0	aug-pc-1	aug-pc-2	aug-pc-3	aug-pc-0	aug-pc-1	aug-pc-2	aug-pc-3	
2A _g	3.64	3.54	3.53	3.53	3.73	3.65	3.64	3.64	
1A _u	3.93	4.11	4.06	4.06	4.01	4.20	4.14	4.13	
1B _{1g}	3.44	3.38	3.38	3.38	3.52	3.48	3.47	3.47	
1B _{1u}	4.03	4.15	4.10	4.11	4.10	4.23	4.16	4.16	
1B _{2g}	4.00	4.14	4.09	4.09	4.05	4.20	4.13	4.13	
2B _{2g}	5.01	4.89	4.88	4.87	5.69	5.59	5.58	5.57	
1B _{2u}	2.29	2.26	2.25	2.25	2.33	2.30	2.29	2.29	1.98
2B _{2u}	3.37	3.29	3.28	3.28	3.43	3.36	3.35	3.34	3.33
3B _{2u}	3.84	3.76	3.75	3.75	3.91	3.85	3.84	3.84	3.65
1B _{3g}	3.91	4.10	4.05	4.05	3.98	4.18	4.11	4.11	
1B _{3u}	2.46	2.40	2.39	2.39	2.51	2.45	2.44	2.44	2.42
2B _{3u}	3.52	3.43	3.41	3.41	3.58	3.49	3.48	3.47	3.33
3B _{3u}	3.78	3.68	3.68	3.67	3.86	3.78	3.77	3.77	3.65

^aExperimental values are given for comparison. ^bFrom ref 68.

Focusing here only on basis-set convergence, aug-pc-2 results are almost converged, whereas the aug-pc-0 values deviate from the aug-pc-3 reference data by up to 0.14 eV. The semi-numerical implementation offers a suitable way to use large basis sets, such as aug-pc-3, even for larger molecules.

8. CONCLUSIONS

The TDDFT exchange-correlation kernel of local hybrid functionals has been derived in a relatively general form, and its first implementation into the quantum-chemical program package TURBOMOLE is reported. Due to the functional form of local hybrids, contributions related to exact exchange cannot be computed analytically, and a semi-numerical integration scheme thus has been applied. The efficiency of the implementation has been improved by using the integral screening approximations of the RIJ-COSX method and by an optimization of the included algebraic routines.

A systematic analysis of the semi-numerical integration scheme showed that satisfying accuracy can be obtained even with relatively small integration grids. The only exception is Rydberg excitations in combination with the use of diffuse basis sets. In that case, diffuse and slightly larger grids have to be applied to achieve the target numerical accuracy of 0.01 eV.

Timings of the new semi-numerical implementation have been compared between local and global hybrid functionals, and for the latter, to a corresponding analytical implementation. Even for linear polyene chains, essentially a worst-case scenario, the semi-numerical algorithm improved upon the analytical one regarding scaling with system size, providing in particular a tremendously better scaling with basis-set size. Only minor differences between timings for local and global hybrid functionals are found.

Hence, TDDFT with local hybrid functionals is computationally competitive in comparison to the widely used global hybrid functionals. Calculations on free-base porphyrine showed that even with a very simple LDA-based local hybrid functional adjusted to ground-state data excitation energies are comparable if not better than B3LYP results. A detailed analysis of the performance of local hybrid functionals of different forms for TDDFT calculations of a larger range of systems and excitation types will be reported in due course.

AUTHOR INFORMATION

Corresponding Authors

*(H.B.) E-mail: hilke.bahmann@tu-berlin.de.

*(M.K.) E-mail: martin.kaupp@tu-berlin.de.

Funding

T.M.M. thanks the state of Berlin for financial support via the NaFöG. Funding within DFG project KA1187/13-1 is acknowledged.

Notes

The authors declare no competing financial interest.

ACKNOWLEDGMENTS

We are grateful to the TURBOMOLE developers consortium for access to the source code. We thank Alexei V. Arbuznikov for helpful and stimulating discussions.

REFERENCES

- (1) Dreuw, A.; Head-Gordon, M. *Chem. Rev.* **2005**, *105*, 4009–4037.
- (2) Reining, L.; Olevano, V.; Rubio, A.; Onida, G. *Phys. Rev. Lett.* **2002**, *88*, 066404.
- (3) Onida, G.; Reining, L.; Rubio, A. *Rev. Mod. Phys.* **2002**, *74*, 601–659.
- (4) Sharma, S.; Dewhurst, J. K.; Sanna, A.; Gross, E. K. U. *Phys. Rev. Lett.* **2011**, *107*, 186401.
- (5) Sharma, S.; Dewhurst, J. K.; Shallcross, S.; Madjarova, G. K.; Gross, E. K. U. *J. Chem. Theory Comput.* **2015**, *11*, 1710–1714.
- (6) Weiss, H.; Ahlrichs, R.; Häser, M. *J. Chem. Phys.* **1993**, *99*, 1262–1270.
- (7) Bauernschmitt, R.; Ahlrichs, R.; Hennrich, F. H.; Kappes, M. M. *J. Am. Chem. Soc.* **1998**, *120*, 5052–5059.
- (8) Tozer, D. J.; Handy, N. C. *J. Chem. Phys.* **1998**, *109*, 10180–10189.
- (9) Tozer, D. J.; Handy, N. C. *Phys. Chem. Chem. Phys.* **2000**, *2*, 2117–2121.
- (10) Dreuw, A.; Head-Gordon, M. *J. Am. Chem. Soc.* **2004**, *126*, 4007–4016.
- (11) Becke, A. D. *J. Chem. Phys.* **1993**, *98*, 1372–1377.
- (12) Durant, J. L. *Chem. Phys. Lett.* **1996**, *256*, 595–602.
- (13) Chermette, H.; Razafinjanahary, H.; Carrión, L. *J. Chem. Phys.* **1997**, *107*, 10643–10651.
- (14) Jacquemin, D.; Wathelet, V.; Perpète, E. A.; Adamo, C. *J. Chem. Theory Comput.* **2009**, *5*, 2420–2435.
- (15) Peach, M. J. G.; Benfield, P.; Helgaker, T.; Tozer, D. J. *J. Chem. Phys.* **2008**, *128*, 044118.

- (16) Besley, N.; Peach, M. J. G.; Tozer, D. J. *Phys. Chem. Chem. Phys.* **2009**, *11*, 10350–10358.
- (17) Nakata, A.; Imamura, Y.; Ostuka, T.; Nakai, H. *J. Chem. Phys.* **2006**, *124*, 094105.
- (18) Stoll, H.; Savin, A. In *Density Functional Methods in Physics*; Dreizler, R. M., da Providencia, J., Eds.; Plenum: New York, 1985; pp 177–208.
- (19) Savin, A.; Flad, H.-J. *Int. J. Quantum Chem.* **1995**, *56*, 327–332.
- (20) Iikura, H.; Tsuneda, T.; Yanai, T.; Hirao, K. *J. Chem. Phys.* **2001**, *115*, 3540–3544.
- (21) Tawada, Y.; Tsuneda, T.; Yanagisawa, S.; Yanai, T.; Hirao, K. *J. Chem. Phys.* **2004**, *120*, 8425–8433.
- (22) Vydrov, O. A.; Scuseria, G. E. *J. Chem. Phys.* **2006**, *125*, 234109.
- (23) Heyd, J.; Scuseria, G. E.; Ernzerhof, M. *J. Chem. Phys.* **2003**, *118*, 8207–8215.
- (24) Yanai, T.; Tew, D. P.; Handy, N. C. *Chem. Phys. Lett.* **2004**, *393*, 51–57.
- (25) Chai, J.-D.; Head-Gordon, M. *Phys. Chem. Chem. Phys.* **2008**, *10*, 6615–6620.
- (26) Mardirossian, N.; Parkhill, J. A.; Head-Gordon, M. *Phys. Chem. Chem. Phys.* **2011**, *13*, 19325–19337.
- (27) Toulouse, J.; Colonna, F.; Savin, A. *Phys. Rev. A: At., Mol., Opt. Phys.* **2004**, *70*, 062505.
- (28) Körzdörfer, T.; Sears, J. S.; Sutton, C.; Brédas, J. J. *J. Chem. Phys.* **2011**, *135*, 204107.
- (29) Karolewski, A.; Kronik, L.; Kümmel, S. *J. Chem. Phys.* **2013**, *138*, 204115.
- (30) Jacquemin, D.; Moore, B., II; Planchat, A.; Adamo, C.; Autschbach, J. *J. Chem. Theory Comput.* **2014**, *10*, 1677–1685.
- (31) Cruz, F. G.; Lam, K.-C.; Burke, K. *J. Phys. Chem. A* **1998**, *102*, 4911–4917.
- (32) Jaramillo, J.; Scuseria, G. E.; Ernzerhof, M. *J. Chem. Phys.* **2003**, *118*, 1068–1073.
- (33) Kaupp, M.; Bahmann, H.; Arbuznikov, A. V. *J. Chem. Phys.* **2007**, *127*, 194102.
- (34) Arbuznikov, A. V.; Kaupp, M. *J. Chem. Phys.* **2012**, *136*, 014111.
- (35) Arbuznikov, A. V.; Kaupp, M. *Int. J. Quantum Chem.* **2011**, *111*, 2625–2638.
- (36) Bahmann, H.; Kaupp, M. *J. Chem. Theory Comput.* **2015**, *11*, 1540–1548.
- (37) Ko, C.; Malick, D. K.; Braden, D. A.; Friesner, R. A.; Martinez, T. J. *J. Chem. Phys.* **2008**, *128*, 104103.
- (38) Petrenko, T.; Kossmann, S.; Neese, F. *J. Chem. Phys.* **2011**, *134*, 054116.
- (39) Casida, M. E. In *Recent Advances in Density Functional Methods, Part I*; Chong, D. P., Ed.; World Scientific: Singapore, 1995; pp 155–192.
- (40) Bauernschmitt, R.; Ahlrichs, R. *Chem. Phys. Lett.* **1996**, *256*, 454–464.
- (41) Bates, J. E.; Furche, F. *J. Chem. Phys.* **2012**, *137*, 164105.
- (42) Arbuznikov, A. V.; Kaupp, M.; Bahmann, H. *J. Chem. Phys.* **2006**, *124*, 204102.
- (43) Hirata, S.; Head-Gordon, M.; Bartlett, R. J. *J. Chem. Phys.* **1999**, *111*, 10774–10786.
- (44) Zahariev, F.; Leang, S. S.; Gordon, M. S. *J. Chem. Phys.* **2013**, *138*, 244108.
- (45) Neese, F.; Wennmohs, F.; Hansen, A.; Becker, U. *Chem. Phys.* **2009**, *356*, 98–109.
- (46) Friesner, R. A. *Chem. Phys. Lett.* **1985**, *116*, 39–43.
- (47) Friesner, R. A. *Annu. Rev. Phys. Chem.* **1991**, *42*, 341–367.
- (48) Plessow, P.; Weigend, F. *J. Comput. Chem.* **2012**, *33*, 810–816.
- (49) Helgaker, T.; Jørgensen, P.; Olsen, J. *Molecular Electronic-Structure Theory*; John Wiley & Sons: New York, 2000; Chapter 9, pp 336–432.
- (50) Ochsenfeld, C.; White, C. A.; Head-Gordon, M. *J. Chem. Phys.* **1998**, *109*, 1663–1669.
- (51) Izsak, R.; Neese, F.; Klopper, W. *J. Chem. Phys.* **2013**, *139*, 094111.
- (52) van Wüllen, C. *Chem. Phys. Lett.* **1995**, *245*, 648–652.
- (53) Eichkorn, K.; Treutler, O.; Öhm, H.; Häser, M.; Ahlrichs, R. *Chem. Phys. Lett.* **1995**, *240*, 283–290.
- (54) Bauernschmitt, R.; Häser, M.; Treutler, O.; Ahlrichs, R. *Chem. Phys. Lett.* **1997**, *264*, 573–578.
- (55) Weigend, F. *Phys. Chem. Chem. Phys.* **2002**, *4*, 4285–4291.
- (56) Rappoport, D.; Furche, F. *J. Chem. Phys.* **2005**, *122*, 064105.
- (57) Bahmann, H.; Rodenberg, A.; Arbuznikov, A. V.; Kaupp, M. *J. Chem. Phys.* **2007**, *126*, 011103.
- (58) Treutler, O.; Ahlrichs, R. *J. Chem. Phys.* **1995**, *102*, 346–353.
- (59) Becke, A. D. *J. Chem. Phys.* **1988**, *88*, 2547–2553.
- (60) Schreiber, M.; Silva-Junior, M. R.; Sauer, S. P.; Thiel, W. *J. Chem. Phys.* **2008**, *128*, 134110.
- (61) Dunning, T. H., Jr. *J. Chem. Phys.* **1989**, *90*, 1007–1023.
- (62) Dunning, T. H., Jr. *J. Chem. Phys.* **1970**, *53*, 2823–2833.
- (63) Becke, A. D. *J. Chem. Phys.* **1993**, *98*, 5648–5652.
- (64) Perun, S.; Tatchen, J.; Marian, C. M. *ChemPhysChem* **2008**, *9*, 282–292.
- (65) Jensen, F. *J. Chem. Phys.* **2001**, *115*, 9113–9125.
- (66) Jensen, F. *J. Chem. Phys.* **2002**, *117*, 9234–9240.
- (67) Jensen, F. *J. Chem. Phys.* **2002**, *116*, 7372–7379.
- (68) Parusel, A. B. J.; Ghosh, A. *J. Phys. Chem. A* **2000**, *104*, 2504–2507.
- (69) Arbuznikov, A. V.; Kaupp, M. *J. Chem. Phys.* **2008**, *128*, 214107.